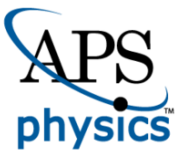

Deformation of a single red blood cell in bounded Poiseuille flows

Lingling Shi, Tsorng-Whay Pan, and Roland Glowinski

Phys. Rev. E **85**, 016307 — Published 10 January 2012

DOI: 10.1103/PhysRevE.85.016307

Deformation of a Single Red Blood Cell in Bounded Poiseuille Flows

Lingling Shi , Tsorng-Whay Pan*, Roland Glowinski
Department of Mathematics, University of Houston, Houston, TX 77204, USA

Abstract

Deformation of red blood cell (RBC) in bounded two dimensional Poiseuille flows is studied by using an immersed boundary method (IBM). An elastic spring model is applied to simulate the skeleton structure of RBC membrane. As a benchmarking test, the dynamical behavior of a single RBC under a simple shear flow has been validated. Then we focus on investigating the motion and the deformation of a single RBC in Poiseuille flows by varying the swelling ratio (s^*), the initial angle of the long axis of the cell at the centerline (φ), the maximum velocity at the centerline of fluid flow (u_{max}), the membrane bending stiffness of RBC (k_b) and the height of the microchannel (H). Two motions of oscillation and vacillating-breathing (swing) of RBC are observed in both narrow and wide channels. The strength of the vacillating-breathing motion depends on the degree of confinement and the value of u_{max}. RBC exhibits a strong vacillating-breathing motion as the degree of confinement is larger or the value of u_{max} is higher. For the same degree of confinement, the vacillating-breathing motion appears to be relatively weaker but persists longer as the value of u_{max} is lower. The continuation of shape change from the slippery to the parachute by varying the value of u_{max} is obtained for the biconcave shape cell in a narrower channel. In particular, parachute shape and bulletlike shape, depending on the angle φ, coexist for the elliptic shape cell given initially with lower u_{max} in a narrower channel.

Keywords deformation, red blood cell, elastic spring model, immersed boundary method, Poiseuille flow.

1 Introduction

Red blood cell (RBC) membrane composing of a lipid bilayer underlined by a spectrin network of cytoskeletal proteins is highly deformable so that RBC can change its shape when an external force is acting on it and return to the biconcave resting shape after the removal of the force [1]. The normal RBC has a biconcave disk with a major diameter about 8μm and thickness about 2μm as its rest shape. The mean volume is about $90\mu\text{m}^3$ and the average

*Corresponding author. E-mail address: pan@math.uh.edu

surface area of RBC is about 135 μm^2, a value greater than the surface area (97.12 μm^2) of a sphere with the same volume [2]. This excess area also contributes to RBC deformation. This deformability of the RBC membrane makes it can traverse 3μm in diameter capillaries of the microcirculation. The deformation of RBC influences not only its physicological function in oxygen tranport [3] but also the hydrodynamical properties of normal human blood, where the volume fraction of RBCs is about 40-45%. Some diseases such as malaria and anemias are also related with reduced RBC deformation [4, 5].

Starting from the pioneering work of Fahraeus and Lindqvist, the behavior of soft entities, such as capsules, vesicles and blood cells under shear flow has been studied theoretically [6, 7, 8], experimentally [9] and numerically [10, 11, 12, 13, 14, 15] by many researchers in mathematics, physics and mechanics, biology and medcine. Three different types of dynamics have been observed for the vesicles and cells in shear flow: tank-treading (TT) [7, 12, 15, 16], tumbling (TB)[11, 13, 17], and vacillating-breathing (VB) [13, 14]. Motivated by the complex and interesting behavior of the vesicles and cells in shear flow, we focus our attention on exploring the more complex dynamics of a single RBC in Poiseuille flows in this paper.

Several numerical methods have been developed to study the motion and the deformation of cell in microchannels. Coupier et al. studied the noninertial migration of vesicles in bounded Poiseuille flows experimentally and numerically and reported that the movement toward the center of channel is induced by the combined effects of the walls and of the curvature of the velocity profile [18]. Danker et al. investigated the effect of viscosity ratio on migration of vesicles in a Poiseuille flow by theoretical analysis and predicted coexistence of two types of shapes: bulletlike shape and parachutelike shape [19]. Pozrikidis studied the motion of spherical, oblate ellipsoidal and biconcave capsules in tube flow by using boundary element method and observed that spherical capsules slowly migrate to the tube centerline, and oblate and biconcave capsules develop parachute and slipperylike shapes, respectively [20]. Li et al. investigated the shape changes and motion of vesicle by using lattice-Boitzmann method [8]. The asymmetric shape of vesicle in an unbounded Poiseuille flow at zero Reynolds number was studied by Kaoui et al. [21]. In most of these studies, no inertial effect (i.e. the Stokes flow) was considered. Park et al. applied the inertial lift force to particle motions in particle separation experimentally [22]. The oscillatory motion for drops in pressure-driven channel flow at finite Reynolds number by using the boundary integral method has been examined by Mortazavi and Tryggvason [23]. Recently, the inertial migration of elastic capsule in a bounded Poiseuille flow at finite Reynolds number was investigated by Shin [24]. The initial shape of the capsule is either a circle or an ellipse. For the circular initial shape, the equilibrium position can be either at the center of the channel or between the center and the wall (known as the Segre-Silberberg effect) depending on the Reynolds number and the ratio of the capsule size and the channel height. Noguchi and Gompper have studied the shape transition of vesicles and RBCs in capillary flows by employing a three-dimensional mesoscopic simulation method and obtained the slipperylike shape of RBC [25].

In this present paper, the deformation of a single RBC in bounded two dimensional Poiseuille flows is studied by numerical simulation. We use an immersed boundary method combined with the elastic spring model [26] in which the fluid motion is computed by using an operator splitting technique [27, 28, 29] and finite element method [30] with a fixed regular

triangular mesh so that faster solver can be used to solve the fluid flow [15, 31, 32, 33]. The validation of the methodology is presented on the RBC deformation in linear shear flow by comparing with the simulation results using the lattice-Boltzmann method of Kaoui, Harting and Misbah [12]. Then we focus on investigating the deformation of a single RBC in bounded Poiseuille flows. Several factors have been found to be important in determining the deformation of a single RBC in Poiseuille flows: the swelling ratio (s^*), the initial angle of the long axis of the cell at the centerline (φ), the maximum velocity at the centerline of fluid flow (u_{max}), the membrane bending stiffness of RBC (k_b) and the height of the microchannel (H). Two motions of oscillation and vacillating-breathing (also called swing, the long axis undergoes oscillation while the cell shape displays breathing) of RBC are observed in both narrow and wide channels. The strength of the vacillating-breathing motion depends on the degree of confinement and the value of u_{max}. RBC exhibits a strong vacillating-breathing motion as the degree of confinement is larger or the value u_{max} is higher. For the same degree of confinement, the vacillating-breathing motion appears to be relatively weaker but persists longer as the value of u_{max} is lower. For the different bending constants, RBC obtains the same equilibrium shape for the same capillary number $C_a = \mu \mathrm{G_r} {\mathrm{R_0}}^3/\mathrm{B}$, where μ, $\mathrm{G_r}$, $\mathrm{R_0}$ and B represent the plasma viscosity, the shear rate of fluid flow based on the gradient of the velocity at the wall, the effective radius of the cell and the bending coefficient, respectively. The continuation of shape change from the slippery to the parachute by varying the value of u_{max} is obtained for the biconcave shape cell in a narrower channel. In particular, parachute shape and bulletlike shape, depending on the angle φ, coexist for the elliptic shape cell with lower u_{max} in a narrower channel.

The scheme of this paper is as follows: We discuss the elastic spring model and numerical methods in Section 2. In Section 3, we first provide the simulation results on tank-treading under a shear flow as a benchmarking test. Then we present the motion and the deformation of a single RBC in Poiseuille flows and describe the factors affecting the deformation of a single RBC in Poiseuille flows. The conclusions are summarized in Section 4.

2 Model and method

RBC with the viscosity of the cytoplasm same as that of the blood plasma is suspended in a fluid domain Ω filled with blood plasma which is incompressible, Newtonian. Foe some $T > 0$, the governing equations for the fluid-cell system are the Navier-Stokes equations

$$\rho\left(\frac{\partial u}{\partial t} + u \cdot \nabla u\right) = -\nabla p + \mu \triangle u + f, \text{ in } \Omega \times (0, T), \tag{1}$$

$$\nabla \cdot u = 0, \text{ in } \Omega \times (0, T). \tag{2}$$

Equations (1) and (2) are completed by the following boundary and initial conditions:

$$u = g \text{ on the top and bottom of } \Omega \text{ and } u \text{ is periodic in the } x_1 \text{ direction}, \tag{3}$$

$$u(x, 0) = u_0(x), \text{ in } \Omega \tag{4}$$

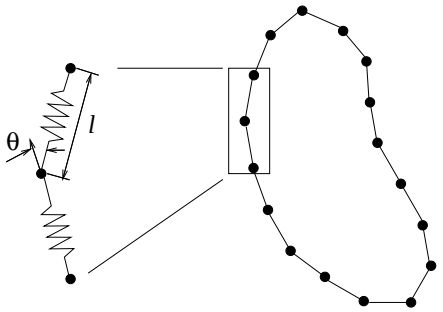

Figure 1: The elastic spring model of the RBC membrane.

where u and p are the fluid velocity and pressure, respectively, anywhere in the flow, ρ is the fluid density, and μ is the fluid viscosity, which is assumed to be constant for the entire fluid. In (1), f is a body force which is the sum of f_p and f_B where f_p is the pressure gradient pointing in the x_1 direction and f_B accounts for the force acting on the fluid/cell interface. In (4), $u_0(x)$ is the initial fluid velocity. For the cases of shear flow, f_p is set to be zero. When considering Poiseuille flow, we have $g = 0$.

In this paper, the Navier-Stokes equations for fluid flow have been solved by using an operator splitting technique [27, 28, 29] and finite element method [30] with a regular triangular mesh so that the faster solver from FISHPAK by Adams et al. [34] can be used to solve the fluid flow. The motion of the RBCs in the fluid flow is simulated by combining the immersed boundary method [35, 36, 37] and the elastic spring model for RBC membrane [26](see [15, 32, 33]).

2.1 Elastic spring model for the RBC membrane

The deformability and the elasticity of the RBC are due to the skeleton architecture of the membrane. A two-dimensional elastic spring model used in [26] is considered in this paper to describe the deformable behavior of the RBCs. Based on this model, the RBC membrane can be viewed as membrane particles connecting with the neighboring membrane particles by springs, as shown in Figure 1. Energy stores in the spring due to the change of the length l of the spring with respect to its reference length l_0 and the change in angle θ between two neighboring springs. The total energy of the RBC membrane, $E = E_l + E_b$, is the sum of the total energy for stretch/compression and the total energy for the bending which, in particular, are

$$E_l = \frac{k_l}{2} \sum_{i=1}^{N} (\frac{l_i - l_0}{l_0})^2 \tag{5}$$

and

$$E_b = \frac{k_b}{2} \sum_{i=1}^{N} tan^2(\theta_i/2). \tag{6}$$

In equations (5) and (6), N is the total number of the spring elements, and k_l and k_b are spring constants for changes in length and bending angle, respectively.

In the process of creating the initial shape of RBCs described in [26], the RBC is assumed to be a circle of radius $R_0 = 2.8$ μm initially. The circle is discretized into $N = 76$ membrane particles so that 76 springs are formed by connecting the neighboring particles. The shape change is stimulated by reducing the total area of the circle through a penalty function

$$\Gamma_s = \frac{k_s}{2}(\frac{s - s_e}{s_e})^2 \tag{7}$$

where s and s_e are the time dependent area of the RBC and the equilibrium area of the RBC, respectively, and the total energy is modified as $E + \Gamma_s$. Based on the principle of virtual work the force acting on the ith membrane particle now is

$$\mathbf{F}_i = -\frac{\partial(E + \Gamma_s)}{\partial \mathbf{r}_i} \tag{8}$$

where $\mathbf{r}_i$ is the position of the ith membrane particle. When the area is reduced, each RBC membrane particle moves on the basis of the following equation of motion:

$$m\ddot{\mathbf{r}}_i + \gamma\dot{\mathbf{r}}_i = \mathbf{F}_i \tag{9}$$

Here, $\dot{()}$ denotes the time derivative; m and γ represent the membrane particle mass and the membrane viscosity of the RBC. The position $\mathbf{r}_i$ of the ith membrane particle is solved by discretizing (9) via a second order finite difference method. The total energy stored in the membrane decreases as the time elapses. The final shape of the RBC is obtained as the total energy is minimized [15]. The area of the final shape has less than 0.001% difference from the given equilibrium area s_e and the length of the perimeter of the final shape has less than 0.005% difference from the circumference of the initial circle. The value of the swelling ratio of a RBC in this paper is defined by $s^* = s_e/(\pi R_0^2)$.

2.2 Immersed boundary method

The immersed boundary method developed by Peskin, e.g, [35, 36, 37], is employed in this study because of its distinguish features in dealing with the problem of fluid flow interacting with a flexible fluid/structure interface. Based on the method, the boundary of the deformable structure is discretized spatially into a set of boundary nodes. The force located at the immersed boundary node $\mathbf{X} = (X_1, X_2)$ affects the nearby fluid mesh nodes $\mathbf{x} = (x_1, x_2)$ through a 2D discrete δ-function $D_h(\mathbf{X} - \mathbf{x})$:

$$\mathbf{f}_B(\mathbf{x}) = \sum \mathbf{F}_i D_h(\mathbf{X}_i - \mathbf{x}) \quad \text{for } |\mathbf{X} - \mathbf{x}| \leq 2h, \tag{10}$$

where h is the uniform finite element mesh size and

$$D_h(\mathbf{X} - \mathbf{x}) = \delta_h(X_1 - x_1)\delta_h(X_2 - x_2) \tag{11}$$

with the 1D discrete δ-functions being

$$\delta_h(z) = \begin{cases} \frac{1}{8h}\left(3 - 2|z|/h + \sqrt{1 + 4|z|/h - 4(|z|/h)^2}\right), & |z| \le h, \\ \frac{1}{8h}\left(5 - 2|z|/h - \sqrt{-7 + 12|z|/h - 4(|z|/h)^2}\right), & h \le |z| \le 2h, \\ 0, & \text{otherwise.} \end{cases} \tag{12}$$

The movement of the immersed boundary node $\mathbf{X}$ is also affected by the surrounding fluid and therefore is enforced by summing the velocities at the nearby fluid mesh nodes $\mathbf{x}$ weighted by the same discrete δ-function:

$$\mathbf{U}(\mathbf{X}) = \sum h^2 \mathbf{u}(\mathbf{x}) D_h(\mathbf{X} - \mathbf{x}) \quad for \ \ |\mathbf{X} - \mathbf{x}| \le 2h. \tag{13}$$

After each time step, the position of the immersed boundary node is updated by

$$\mathbf{X}_{t+\Delta t} = \mathbf{X}_t + \Delta t \mathbf{U}(\mathbf{X}_t). \tag{14}$$

Remark. At each time step, via operator splitting, we solve a sequence of subproblems, namely a degenerated quasi-Stokes problem, the membrane motion, the advection problem and the diffusion problem as in [33]. We keep the conservation of area given in (7) when computing membrane force in (8) since the divergence free condition is enforced in a weak sence through the finite element method used in the computations.

3 Simulation results and discussions

In [15], we have validated the elastic spring model and achieved the cells equilibrium shapes for different values of the swelling ratio s^* by minimizing the total energy. In this paper, as a benchmarking test, the steady inclination angles of the tank-treading of two different degrees of confinement, the ratio of the cell's effective radius R_0 to the channel half height w, for five values s^* in shear flow are shown and compared with the simulation results in [12]. Then the motion and the deformation of a single RBC in Poiseuille flows has been investigated by varying the swelling ratio (s^*), the initial angle of the long axis of the cell at the centerline (φ), the maximum velocity at the centerline of fluid flow (u_{max}), the membrane bending constant of RBC (k_b) and the height of the microchannel (H). Two motions of oscillation and vacillating-breathing (swing) of RBC are observed in both narrow and wide channels. The continuation of shape change from the slippery to the parachute by varying the value of u_{max} is obtained for the biconcave shape cell in a narrower channel. In particular, parachute shape and bulletlike shape, depending on the angle φ, coexist for the elliptic shape cell with lower u_{max} in a narrower channel.

The values of parameters for modeling cells are same with [32, 33] as follows: The bending constant is $k_b = 5 \times 10^{-10}\mathrm{N} \cdot \mathrm{m}$, the spring constant is $k_l = 5 \times 10^{-8}\mathrm{N} \cdot \mathrm{m}$, and the penalty coefficient is $k_s = 10^{-5}\mathrm{N} \cdot \mathrm{m}$. The cells are suspended in blood plasma which has a density $\rho = 1.00\mathrm{g/cm}^3$ and a dynamical viscosity $\mu = 0.012\mathrm{g/(cm \cdot s)}$. The viscosity ratio which describes the viscosity contrast of the inner and outer fluid of the RBC membrane is fixed

at 1.0. The computational domain is a two dimensional horizontal channel. To obtain a Poiseuille flow, a constant pressure gradient is prescribed as a body force. To produce a shear flow, a Couette flow driven by two walls at the top and bottom which have the same speed but move in directions opposite to each other is applied to the suspension. Different shear rate can be obtained by adjusting the wall speed. In addition, periodic conditions are imposed at the left and right boundary of the domain. The Reynolds number is defined by $Re = \rho UH/\mu$ where U is the average velocity in the channel.

3.1 Tank-treading in shear flow

First, we present the results on simulation of a single RBC suspended in a linear shear flow with shear rate $\gamma = 500/\text{s}$. The dimensions of the computational domain are $112\mu\text{m} \times 7\mu\text{m}$ and $112\mu\text{m} \times 14\mu\text{m}$. The two degrees of confinement are 0.8 for the narrower domain and 0.4 for the wider domain, respectively. The grid resolution for the computational domain is 80 grid points per 10μm. The time step Δt is 1×10^{-5}ms. The initial velocity of the fluid flow is zero everywhere and the initial positions of the mass center of the cell are (56, 3.5) and (56, 7) for the narrower domain and the wider domain, respectively. Figures 2, 3 show the velocity fields and pressures in the region next to the cells for two different degrees of confinement. The blue solid lines in the left figures and the black solid in the right figures represent the cell membrane. In the left figures, the regions with darker color correspond to higher pressure and the lighter regions correspond to lower pressure. The figures of velocity fields indicate that the cells perform tank-treading motion in confined channels. The streamlines demonstrate that the inner fluid of the cell undergoes a rotational flow, which is induced by the cell membrane tank-treading. The outer fluid of the cell exhibits recirculations at the right side of the figure and at the left side of the figure of the cell. Such recirculations are also observed for confined rotating rigid particles in simple shear flow [11, 38, 39] with period conditions in the shear direction.

The steady inclination angles of the tank-treading of two different degrees of confinement for five values s^*=0.6, 0.7, 0.8, 0.9 and 1.0 are presented in Figure 4, which show the very good agreement with the lattice-Boltzmann simulation results of Kaoui, Harting and Misbah [12]. The inclination angles increases monotonically for both two degrees of confinement with increasing the value of the swelling ratio s^*. For the same swelling ratio, the bigger is the degree of confinement, the smaller is the steady inclination angle. The same qualitative tendency is given in [6, 7, 8, 12, 15, 40]. We also keep track of the area and the perimeter of the cell during the simulations. The variation is less than $\pm 0.1\%$ in the area and $\pm 0.5\%$ in the perimeter.

3.2 Deformation of RBC in Poiseuille flow

3.2.1 Single RBC deformation in a narrow channel

In this section, we focus on investigating the motion and the deformation of a single RBC in Poiseuille flows. First we study how the physical quantities, associated with the lateral migration toward the centerline of the channel for a given maximum velocity at the centerline

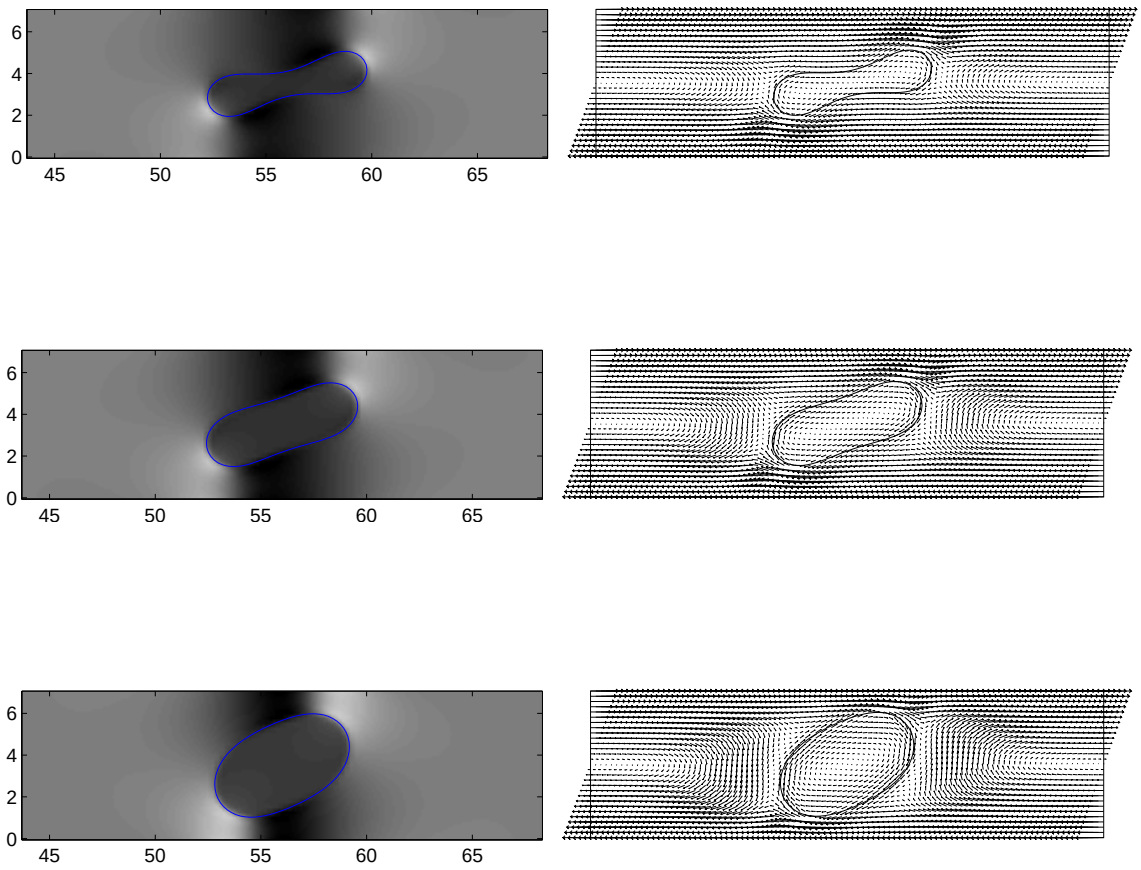

Figure 2: The pressure (left) and the velocity field (right) in the region next to the cell with the swelling ratio s^*=0.481 (top), 0.7 (middle) and 0.9 (bottom), respectively. R_0/w=0.8. The units for both two axes are μm.

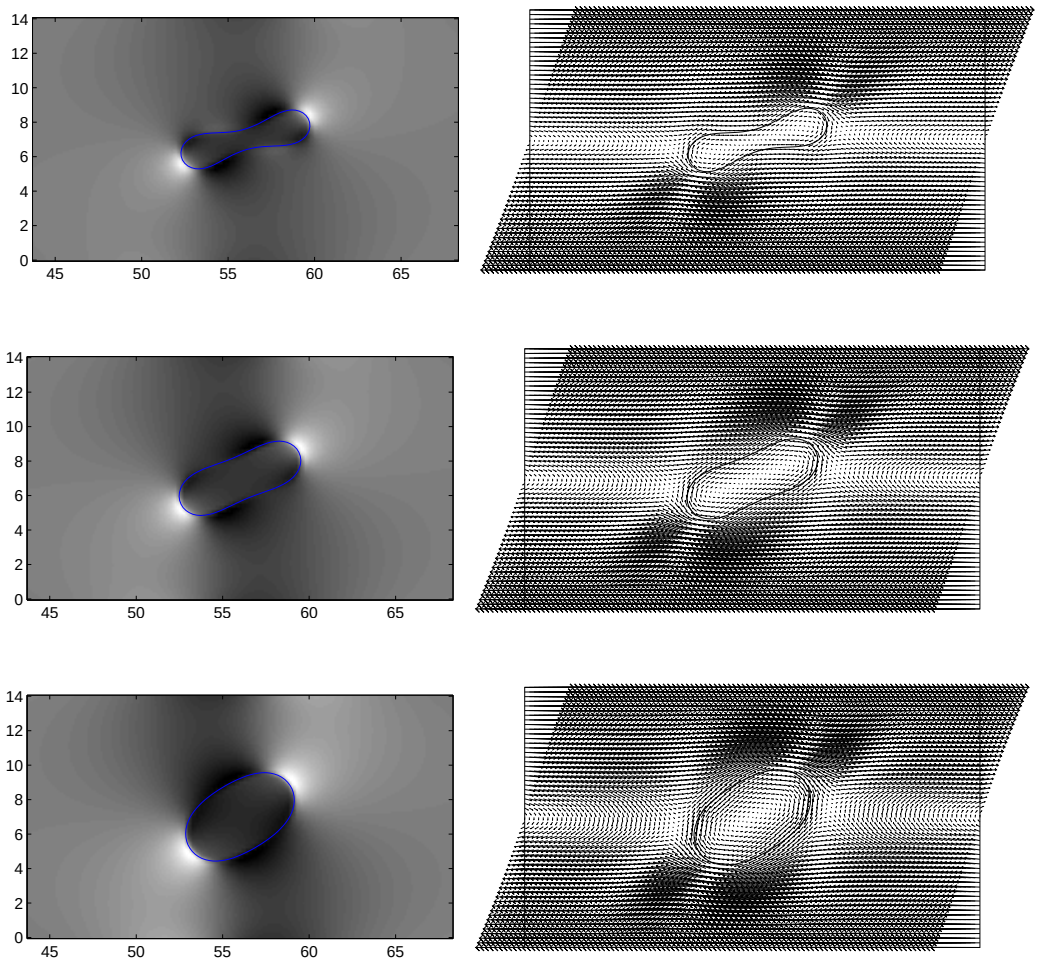

Figure 3: The pressure (left) and the velocity field (right) in the region next to the cell with the swelling ratio s^*=0.481 (top), 0.7 (middle) and 0.9 (bottom), respectively. R_0/w=0.4. The units for both two axes are μm.

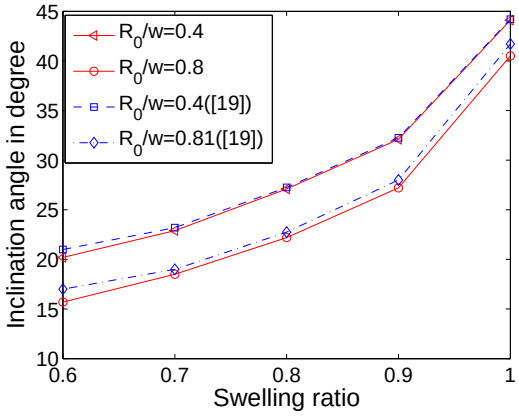

Figure 4: (Color online). Steady inclination angle as a function of the cell swelling ratio for two degrees of confinement R_0/w=0.4 and 0.8.

of fluid flow (u_{max}), vary with the swelling ratio (s^*). Then for two given swelling ratios of biconcave shape s^*=0.481 and elliptic shape s^*=0.9, respectively, we analyze that the effect of the initial position, the initial angle of the long axis of the cell at the centerline (φ), the maximum velocity at the centerline of fluid flow (u_{max}) , the membrane bending stiffness of RBC (k_b), and the height of the microchannel (H) on the deformation of RBC. Two motions of oscillation and vacillating-breathing (swing) of RBC are observed in both narrow and wide channels. The continuation of shape change from the slippery to the parachute by varying the value of u_{max} is obtained for the biconcave shape cell in a narrower channel. In particular, parachute shape and bulletlike shape, depending on the angle φ, coexist for the elliptic shape cell with lower u_{max} in a narrower channel.

3.2.1.1 Effect of the swelling ratio

We first present the simulation results of a single RBC in a Poiseuille flow with the fluid domain 100μm $\times$ 10μm. The pressure gradient is set to as a constant for this study so that the Reynolds number of the Poiseuille flow without cell is about 0.4167. The initial velocity is zero everywhere. The grid resolution for the computational domain is 64 points per 10μm. Three different shapes (s^*=0.481, 0.7 and 0.9) have been studied and the results are shown in Figure 5. The initial position of the mass center of the single cell is located at (5,3). The initial angle of the long axis of the cell at the centerline is φ=0. In Figure 5, the cells deform and migrate to the centerline of the microchannel and the well-known parachute shape has been observed for the case of s^*=0.481, 0.7 and 0.9. The red asterisk denotes the same point on the cell membrane for the entire simulation. The similar results of capsules in tube flow using the boundary element method have been reported by Pozrikidis in [20].

Given the same initial angle of the long axis of the cell at the centerline φ=0, the effect of different initial positions has been investigated. Migrations of RBC with s^*=0.481 and 0.9 for three different initial positions (5,3), (5,5) and (5,7.7) are shown in Figure 6. The

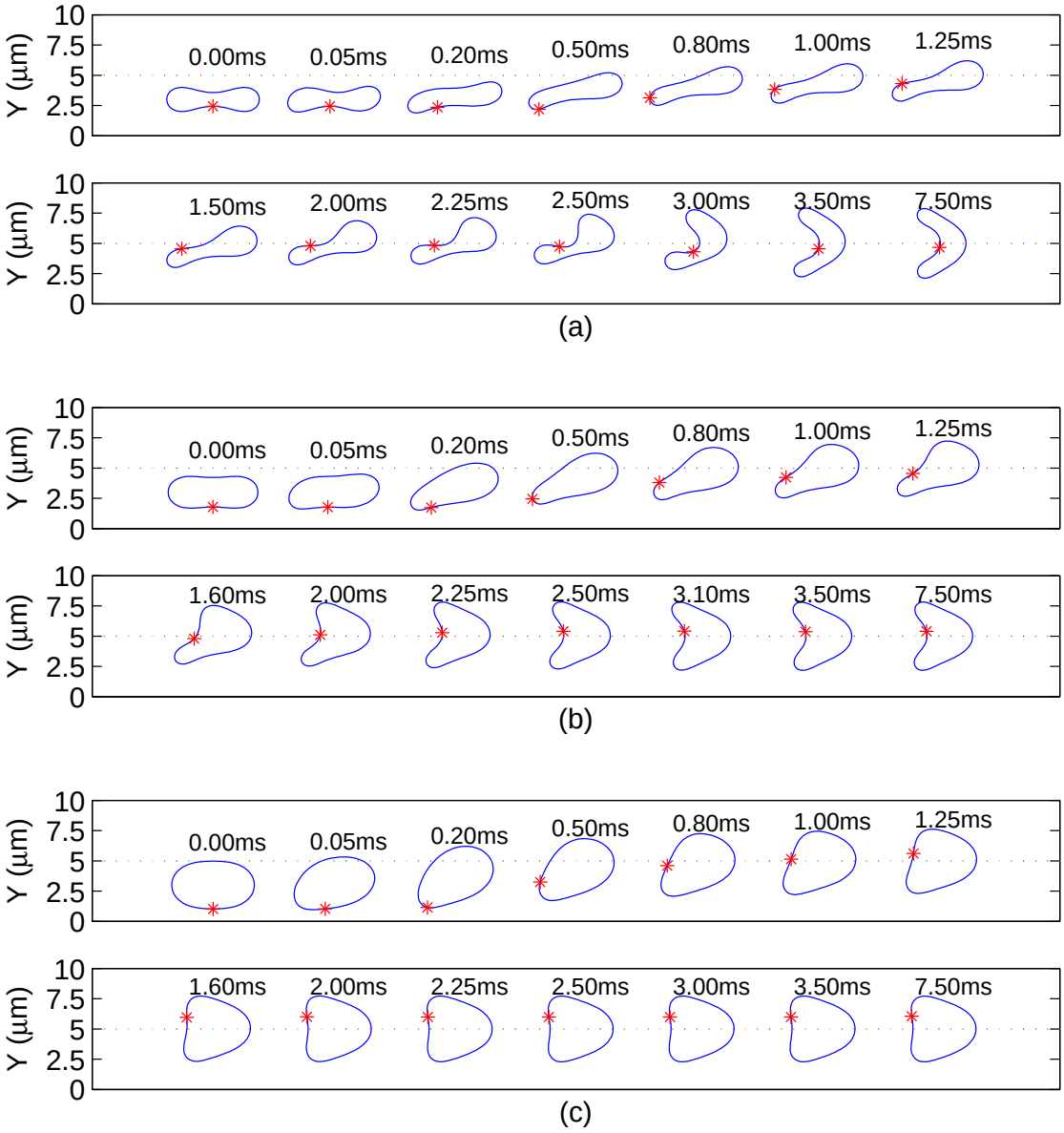

Figure 5: (Color online). The snapshots of the cell migration in a Poiseuille flow: $(a)s^*$=0.481, $(b)s^*$=0.7 and $(c)s^*$=0.9. The red asterisk denotes the same node point on the cell membrane.

cells with the initial positions (5,3) and (5,7.7) deform and migrate to the centerline of the microchannel where steady axisymmetric states are reached. The cell with the initial position (5,5) parallels to the direction of the flow after it is released, then deforms owing to the hydrodynamic stress imposed symmetrically by the Poiseuille flow, until reaches the parachute shape as its equilibrium shape. The final position and shape are not related with the initial positions of the RBC.

3.2.1.2 Effect of the initial angle of the long axis of the cell at the centerline

The initial angle of the long axis of the cell at the centerline φ has important effect on the equilibrium position and shape for the elliptic shape cell with s^*=0.9. Two equilibrium shapes, parachute shape and bulletlike shape, coexist at the centerline as equilibrium shapes for u_{max}=1.0 cm/s with different initial inclination angles φ (see Figure 7). When φ is bigger than 37°, the parachute shape is obtained, otherwise the bulletlike shape is obtained. The similar qualitative results of the cell in an unbounded Stokes flow has been reported in [19]. The averaged velocities of the fluid with cell are 0.653 cm/s for the cell type I (bulletlike shape) and 0.642 cm/s for the cell type II (parachute shape), respectively, and the energy stored in the membrane of the cell type I is lower than that of the cell type II. That's because the resistance force acted on the fluid by the cell type I is less than the force by the cell type II. This resistance force depends on the cell cross-section perpendicular to the direction of fluid flow in a narrow channel and the velocity of quadratic flow without cell. Then the inverse force acted on the cell type I by the fluid is less than the inverse force acted on the cell type I by the fluid. This interplay between the fluid and the cell is the main source of the energy stored in the membrane.

However, for the biconcave shape cell s^*=0.481, only slippery shape has been obtained at the centerline as its equilibrium shape for u_{max}=1.0 cm/s with the initial inclination angle of $0°, 45°$,and 90° as shown in Figure 8. It indicates that slippery shape could be the only equilibrium shape for the low u_{max}.

3.2.1.3 Effect of the maximum velocity at the centerline of fluid flow

The effect of u_{max} on the deformation of a single cell has been investigated. In the simulations, we have kept other parameters same as in Section 3.2.1.1. We observed that u_{max} plays a critical role on the equilibrium shapes of a single RBC migration in a narrow channel. Both slippery shape and parachute shape are obtained by varying the value of u_{max}. The slippery shape is obtained when u_{max} is lower than a critical value $u_c = 3$ cm/s (resp., 2.8 cm/s) for s^*=0.481 (resp., 0.7), and the parachute shape is obtained when u_{max} is higher than u_c. The asymmetric shape (slipperylike shape) of vesicle in an unbounded Poiseuille flow at zero Reynolds number has been studied by Kaoui et al [21], and the similar results of vesicle also mentioned in [41, 42, 43]. Figure 9 shows that the equilibrium shapes for s^*=0.481 and 0.7 with nine different values of u_{max} =0.5, 1.0, 1.5, 2.0, 2.5, 2.8, 3.0, 4.0, 7.5 cm/s, and the corresponding Reynolds numbers of the Poiseuille flow without cell are about 0.0278, 0.0556, 0.0833, 0.1111, 0.1389, 0.1556, 0.1667, 0.2222, 0.4167, respectively. The histories of the cell membrane energy for s^*=0.481 and 0.7 are shown in Figure 10. When the cell reaches the equilibrium position and shape, the cell membrane energy of the

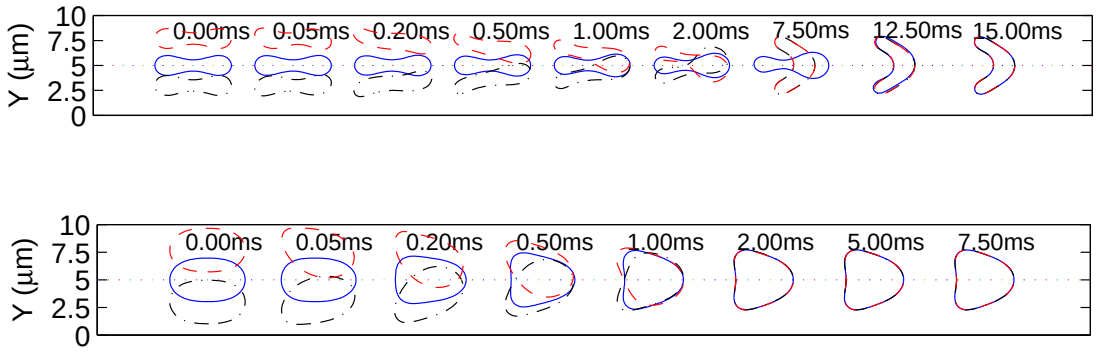

Figure 6: (Color online). The snapshots of the cell migration with s^*=0.481(top) and 0.9(bottom) in a Poiseuille flow for three different initial positions.

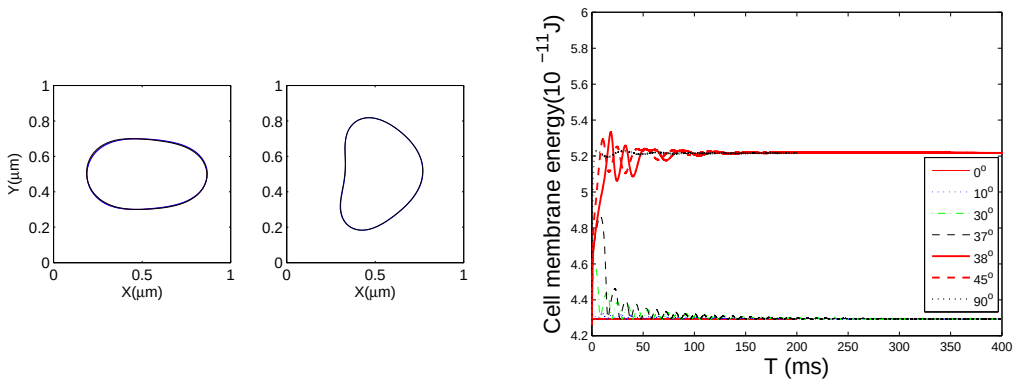

Figure 7: (Color online). Two shapes: bulletlike shape with u_{max}=1cm/s and θ=0°, 10°, 30° and 37°(left) and parachute shape with u_{max}=1cm/s and θ=38°, 40°, 45° and 90° (middle). The histories of cell membrane energy for different initial inclination angles φ (right).

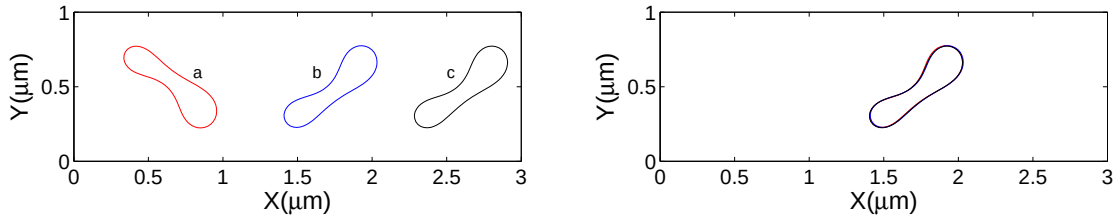

Figure 8: (Color online). The equilibrium shapes for different initial angles:(a) $\theta = 0$, (b)$\theta = 45°$ and (c) $\theta = 90°$(left). The shapes after shifting and reflecting with respect to the centerline of the channel (right). s^*=0.481 and u_{max}=1cm/s.

parachute shape is higher than that of the slippery shape and the flow with higher u_{max} can provide enough energy to sustain the shape of parachute. The distance Y_d between the mass center of equilibrium cell and the centerline is zero for the parachute shape, but Y_d is nonzero for the slippery shape. These results are reported in Figure 11. Our present simulation results are in good agreement with the results in [21].

For the above nine different values of u_{max}, the equilibrium shapes of the elliptic shape cell for s^*=0.9 with two different initial angles $\varphi = \pi/4$ and 0 are shown in Figure 12. For the initial inclination angle $\varphi = 0$, the cell deforms and reaches bulletlike shape as its equilibrium shape when u_{max} is lower than $u_c = 3$ cm/s, otherwise it attains parachute shape. But for the initial inclination angle $\varphi = \pi/4$, the cell deforms and reaches bulletlike shape as its equilibrium shape when u_{max} is between 1.0 cm/s and 3.0 cm/s, otherwise it attains parachute shape. Both bulletlike shape and parachute shape coexist for u_{max} =0.5, 1.0 and 3.0 cm/s. These results indicate that when u_{max} is high enough, the flow can provide enough energy to sustain two different shapes, parachute shape and bulletlike shape, and the final equilibrium shape is determined by other factors such as the initial inclination angle and etc.

We have also applied the method of the numerical continuation to study the change of the equilibrium shape of the cell for $s^* = 0.481$ and 0.7. After obtaining an equilibrium shape for a given value of u_{max}, we have used it as the initial shape in the simulation for the next larger value of u_{max}. The equilibrium shapes for $s^* = 0.481$ and 0.7 are exactly same as those given in Figure 9.

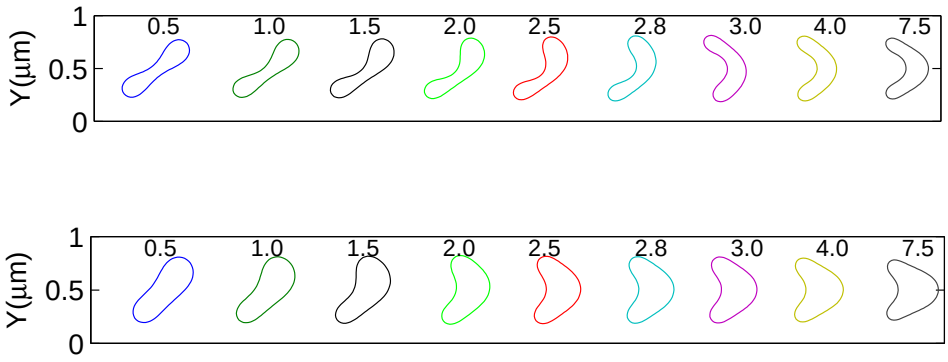

Figure 9: (Color online). The equilibrium shapes of a single cell in a Poiseuille flow for s^*=0.481 (top) and 0.7 (bottom) with u_{max} from 0.5 cm/s to 7.5 cm/s.

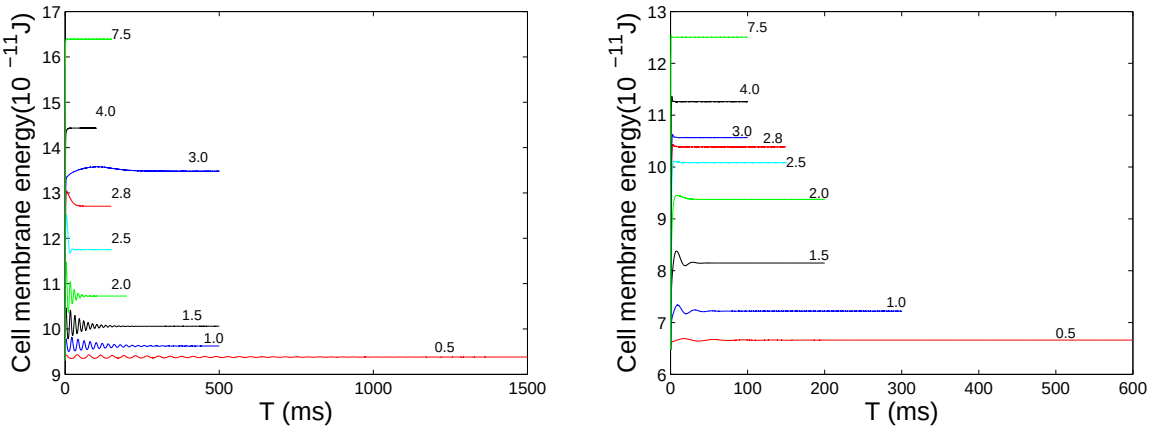

Figure 10: (Color online). The histories of the cell membrane energy in a Poiseuille flow for s^*=0.481(left) and 0.7(right) with u_{max} from 0.5 cm/s to 7.5 cm/s.

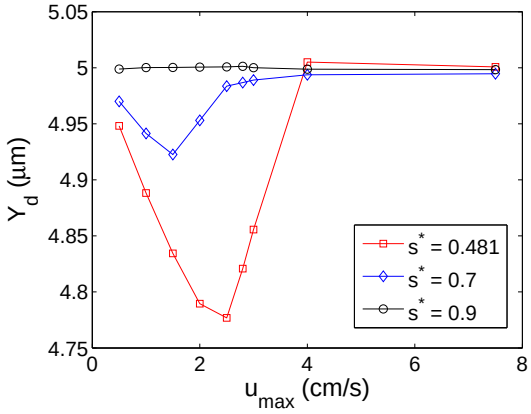

Figure 11: (Color online). The distance Y_d between the mass center of equilibrium cell and the centerline as a function of u_{max} (cm/s).

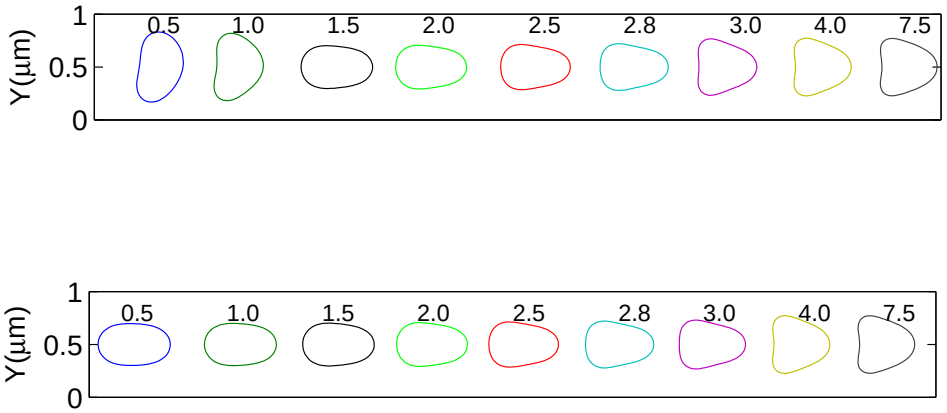

Figure 12: (Color online). The equilibrium shapes of a single cell of $s^* = 0.9$ in a Poiseuille flow with various values of u_{max} (cm/s) for two initial angles: $\varphi = \pi/4$ (top) and 0 (bottom).

3.2.1.4 Effect of the membrane bending stiffness of RBC and the height of the microchannel

To study the effect of the bending constant, we have kept the same values of k_l, k_s and considered three different values of the bending constants, which are $0.1k_b$, $1k_b$ and $10k_b$, $u_{max} = 1.0$ cm/s and other conditions are same as in Section 3.2.1.1. The snapshots of the cell migration in Poiseuille flows for $s^* = 0.481$ and 0.9 with these bending constants are shown in Figure 13 and the histories of the cell membrane energy are reported in Figure 14. In Figure 13, the red asterisk denotes the same point on the cell membrane during the entire simulation. For the lower bending constant $0.1k_b$, parachute shape is obtained for both the biconcave shape cell $s^* = 0.481$ and the elliptic shape cell $s^* = 0.9$. For the bending constant $1k_b$, both two cells exhibit damped oscillating-breathing after they are released in the fluid flow as indicated in Figure 14. The histories of the cell membrane energy show the vacillating-breathing motion of the elliptic shape cell $s^* = 0.9$ damps out faster than that of the biconcave shape cell of $s^* = 0.481$. The positions and shapes of the vacillating-breathing motion for the biconcave shape cell of $s^* = 0.481$ are shown in Figure 15. For the higher bending constant $10k_b$, both two cells exhibit damped oscillation until they attain the equilibrium states aligning themselves at an angle with the direction of the flow, and the damping rate of the elliptical shape cell is bigger than that of the biconcave shape cell. The history of the angle of the long axis of cell at the centerline as a function of time is shown in Figure 16 (left). The vacillating-breathing motion also takes place for the bending constants $0.1k_b$ with the value of u_{max} lower than 1.0 cm/s and $10k_b$ with the value of u_{max} higher than 1.0 cm/s for the biconcave shape cell of $s^* = 0.481$. Figure 17 shows the simulation results of the capillary number $C_a = 3.58$ (i.e., $0.1k_b$ with the value of $u_{max} = 0.1$ cm/s, $1k_b$ with the value of $u_{max} = 1$ cm/s and $10k_b$ with the value of $u_{max} = 10$ cm/s). For the different bending constants, the RBC reaches the same equilibrium shape for the same capillary number in the middle part of Figure 17.

The shear rate at the center of the Poiseuille flow is zero, and any deviation of the cell from the centerline would be penalized by higher dissipation as a result of the higher shear rate. Thus for a parachute shape cell, no membrane tank-treading is present for its symmetric shape and the relative velocity of fluid inside the parachute shape cell also vanishes. However, for a slippery shape cell, its membrane undergoes tank-treading and the flow enclosed by the slippery shape cell rotates as shown in Figure 18 (a) and (c) where the red asterisk denotes the same point on the cell membrane. The similar results of vesicle [21] and elliptical capsule [24] are also obtained by Kaoui et al. and Shin et al., respectively.

Finally, the effect of the height of the channel H on the deformation of a single cell is also investigated. We set u_{max}=7.5 cm/s and vary H. All the other physical and numerical parameters are kept same to those in the Section 3.2.1.1. Simulations in Figure 19 and Figure 20 are performed for $H = 10\mu$m and 50μm, respectively. The corresponding initial positions of the mass center of the single cell are located at (5, 5) and (5, 25), respectively. Both the initial angles of the long axis of the cell at the centerline are $\varphi = \pi/4$. For the narrower channel $H = 10\mu$m, the cell deforms into parachute shape as its equilibrium shape for the bending constants $0.1k_b$ and $1k_b$, and displays vacillating-breathing motion for the bending constant $10k_b$ accompanied by membrane tank-treading for the case of $s^* = 0.481$

as in Figure 19. No tank-treading for both parachute shape and bulletlike shape since the equilibrium shapes are symmetric (see Figure 18 (b) and (d)). Unlike in a narrower channel, the cell in a wider channel exhibits vacillating-breathing motion after it is released in the fluid flow for the lower bending constant $0.1kb$, and as this motion becomes weak, the cell reaches a slippery shape as its equilibrium state aligning itself at an angle with the direction of the flow. For the bending constants $1k_b$ and $10k_b$, both two cells exhibit oscillation. The similar simulation results of vesicles by using boundary integral method are given by Kaoui et al. in [44]. The history of the position of the cell mass center, the energy of the cell membrane, and the equilibrium shape are presented in Figure 20. The histories of the angle of the long axis of the biconcave cell $s^* = 0.481$ at the centerline for the bending constants $1k_b$ and $10k_b$ are shown in Figure 16(right).

RBC exhibits slippery shape accompanied with (damped) vacillating-breathing motion when the capillary number C_a is less than a critical value such as 10.74 for the biconcave shape cell $s^* = 0.481$ in the narrower channel. For the elliptic shape cell of $s^* = 0.9$, the vacillating-breathing motion damps out quickly. So we focus our attention on investigating the vacillating-breathing motion of the biconcave shape cell for $s^* = 0.481$. Figure 21 displays the histories of the energy of the cell membrane of the different values of u_{max}=0.5, 1.0, 1.5, 2.0, 2.8 cm/s. The strength of the vacillating-breathing motion depends on the degree of confinement, the maximum velocity at the centerline of fluid flow u_{max} and the capillary number C_a. RBC exhibits a stronger vacillating-breathing motion as the degree of confinement is larger or the value u_{max} is higher. For the same degree of confinement, the vacillating-breathing motion appears to be relatively weaker but persists longer as the value of u_{max} is lower. For the different bending constants, RBC obtains the same equilibrium shape for the same capillary number.

4 Conclusions

An immersed boundary method combined with the elastic spring model is tested in this paper by reproducing the behavior of RBC under a shear flow. Then we have applied it to study the deformation of a single RBC in bounded Poiseuille flows. Unlike droplet, RBC tends to migrate toward the centerline of the microchannel where an equilibrium state is reached. The steady shape of cell under flow depends on the swelling ratio (s^*), the initial angle of the long axis of the cell at the centerline (φ), the maximum velocity at the centerline of fluid flow (u_{max}), the membrane bending stiffness of RBC (k_b) and the height of the microchannel (H). Two motions of oscillation and vacillating-breathing of RBC are observed in narrow and wide channels. The strength of the vacillating-breathing motion depends on the degree of confinement and the value of u_{max}. RBC exhibits a strong vacillating-breathing motion as the degree of confinement is larger or the value of u_{max} is higher. For the same degree of confinement, the vacillating-breathing motion appears to be relatively weak but persists longer as the value of u_{max} is lower. For the different bending constants, RBC obtains the same equilibrium shape for the same capillary number. The continuation of shape change from the slippery to the parachute by varying the value of u_{max} is obtained for the biconcave shape cell in a narrower channel. In particular, parachute

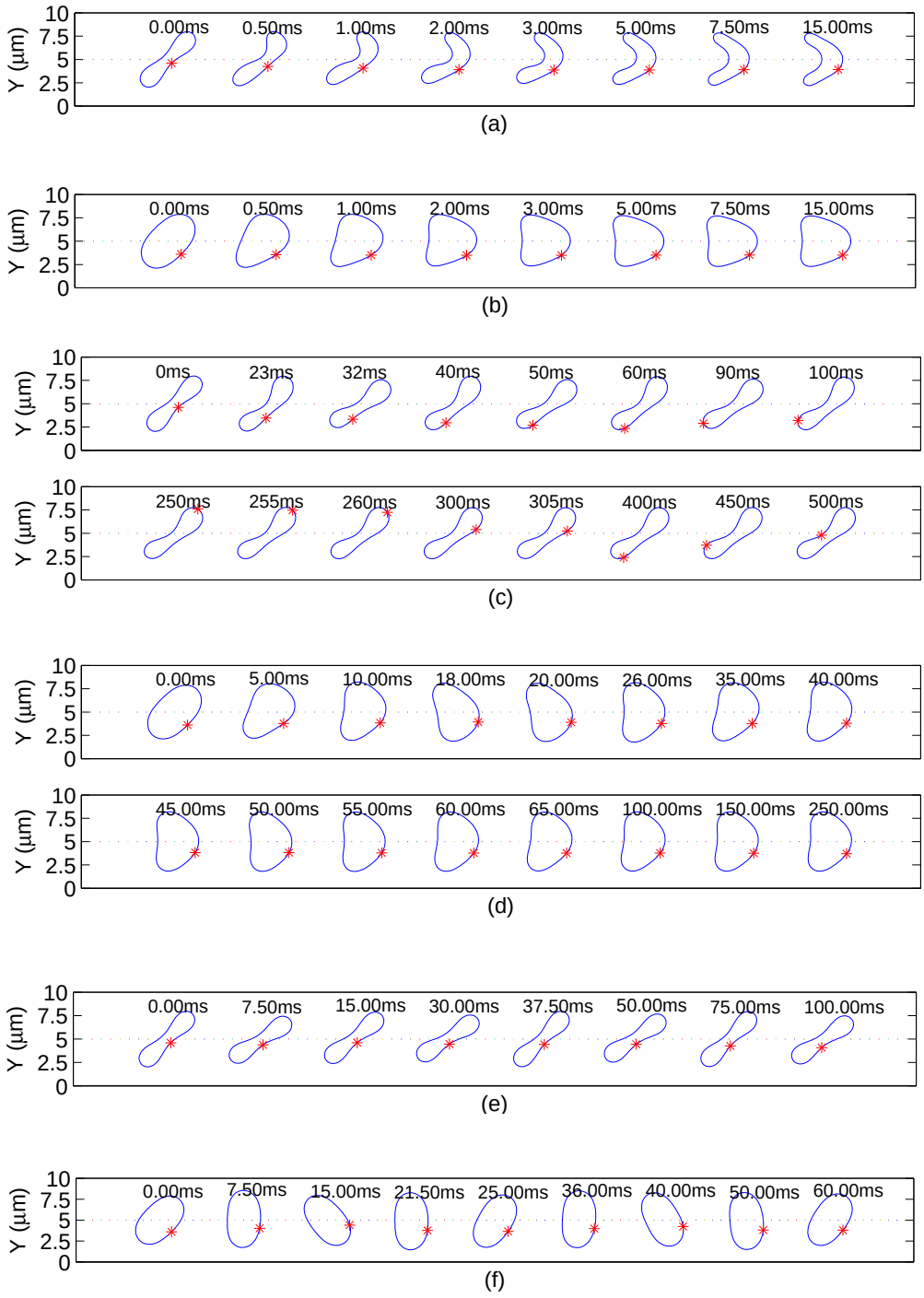

Figure 13: (Color online). The snapshots of the cell migration in Poiseuille flows for $s^* = 0.481$ and 0.9 with different bending constants: (a) $s^* = 0.481$ and $0.1k_b$, (b) $s^* = 0.9$ and $0.1k_b$, (c) $s^* = 0.481$ and $1k_b$, (d) $s^* = 0.9$ and $1k_b$, (e) $s^* = 0.481$ and $10k_b$, and (f) $s^* = 0.9$ and $10k_b$. The red asterisk denotes the same node point on the cell membrane.

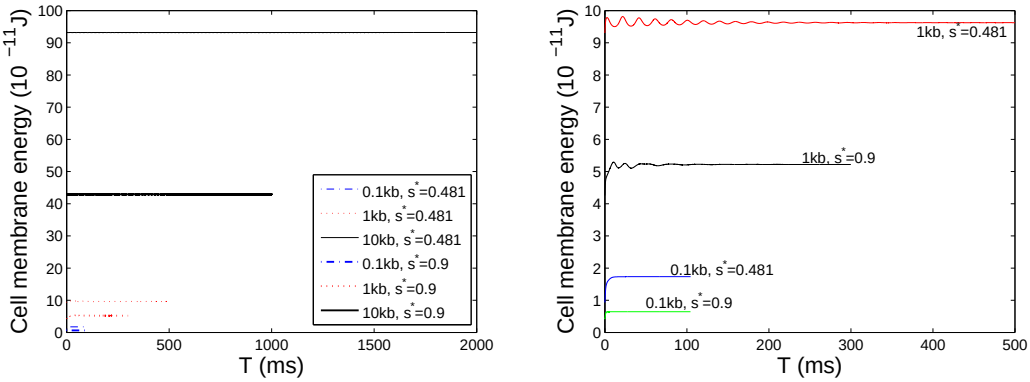

Figure 14: (Color online). The cell membrane energy for $s^* = 0.481$ and 0.9 with different bending constants (left) and the enlarged part (right).

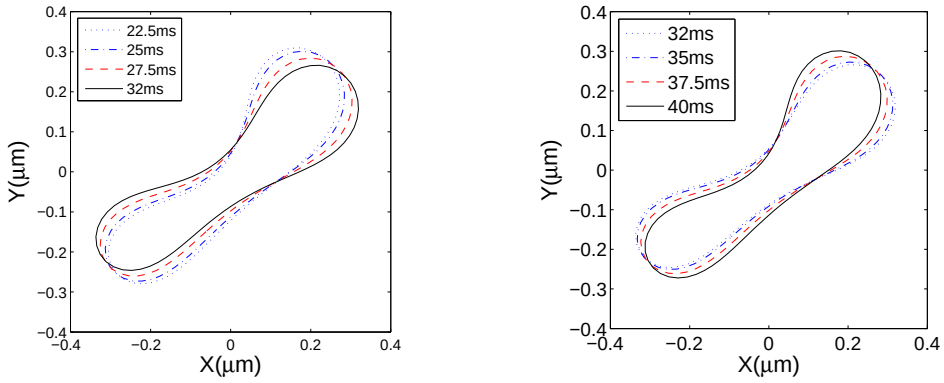

Figure 15: (Color online). The positions and shapes of a single cell for $s^* = 0.481(1k_b)$ at t=22.5, 25, 27.5, 32 ms (left) and t=32, 35, 37.5, 40 ms (right).

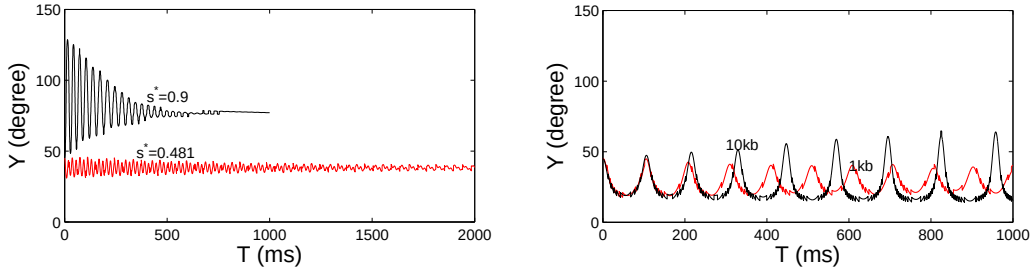

Figure 16: (Color online). The history of the angle of the long axis of cell at the centerline as a function of time: narrower channel (left) and wide channel (right).

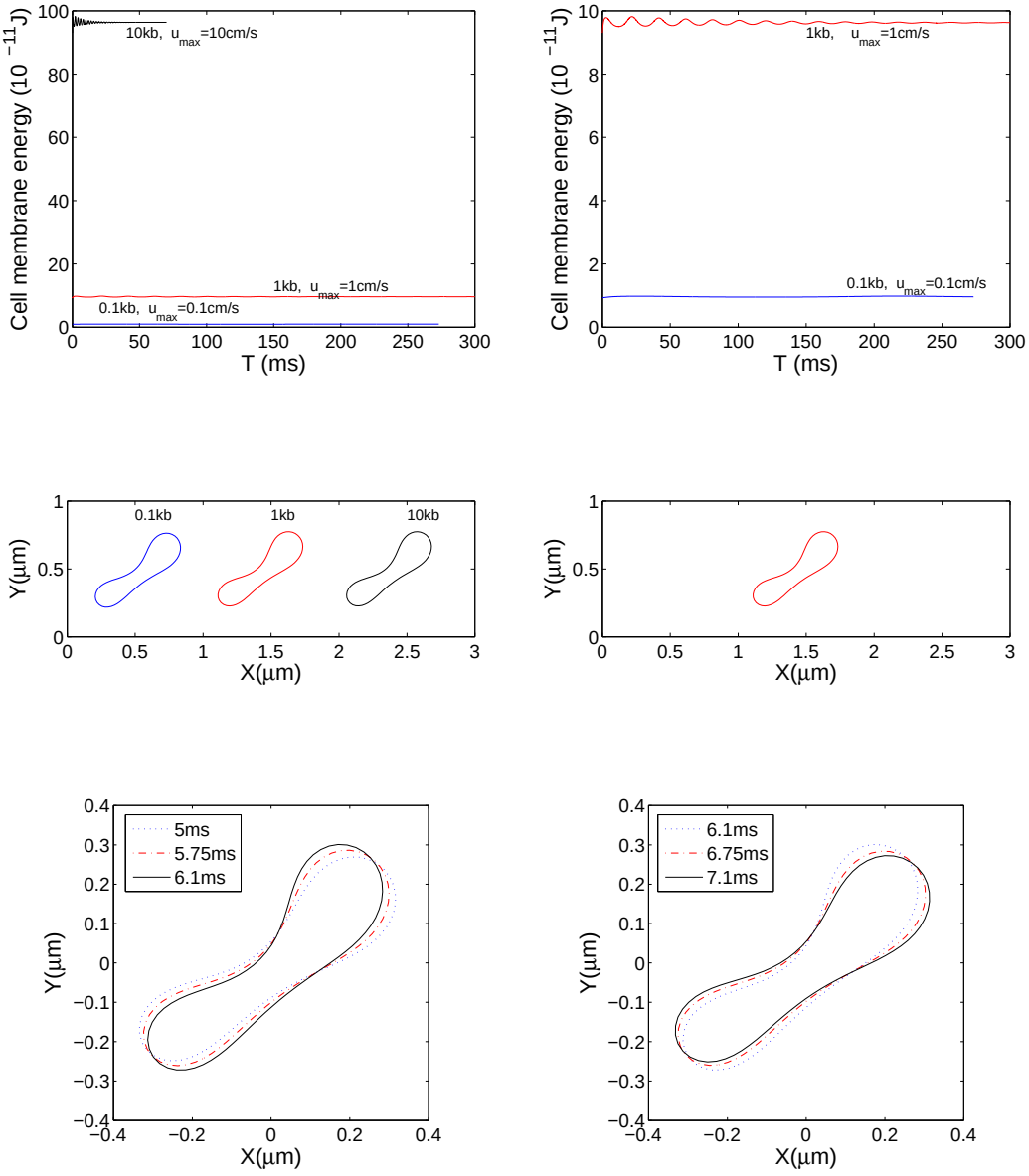

Figure 17: (Color online). The histories of the cell membrane energy for $s^* = 0.481$ with the capillary number $C_a = 3.58$ (top left) and the enlarged part (top right). The equilibrium shapes for different bending constants (middle left) and the shapes after shifting with respect to the centerline of the channel (middle right). The positions and shapes of a single cell for $s^* = 0.481$ ($10k_b$) at t=5, 5.75, 6.1 ms (bottom left) and t =6.1, 6.75 7.1 ms (bottom right).

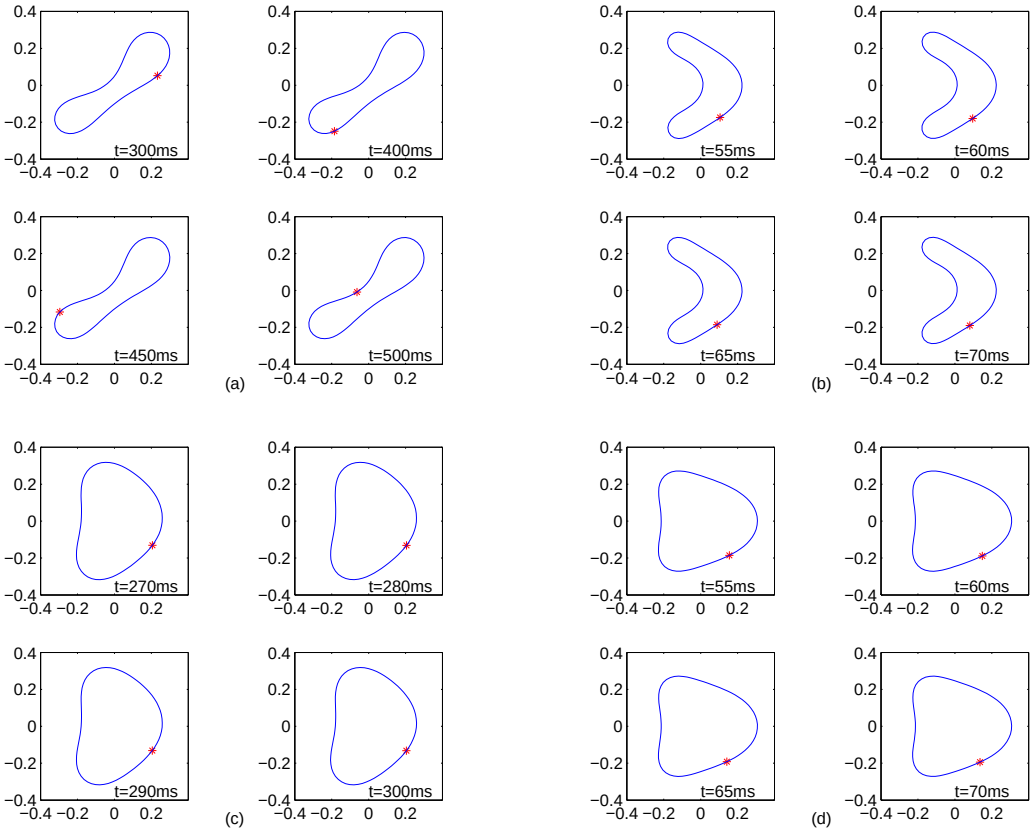

Figure 18: (Color online). Tank treading for a slippery shape cell: (a)s^*=0.481 with u_{max}=1 cm/s. No tank treading for a parachute shape cell: (b) s^*=0.481 with u_{max}=7.5 cm/s, (c)s^*=0.9 with u_{max} = 1 cm/s, and (d) s^*=0.9 with u_{max}=7.5 cm/s. The red asterisk denotes the same node point on the cell membrane. The units for both two axes are μm.

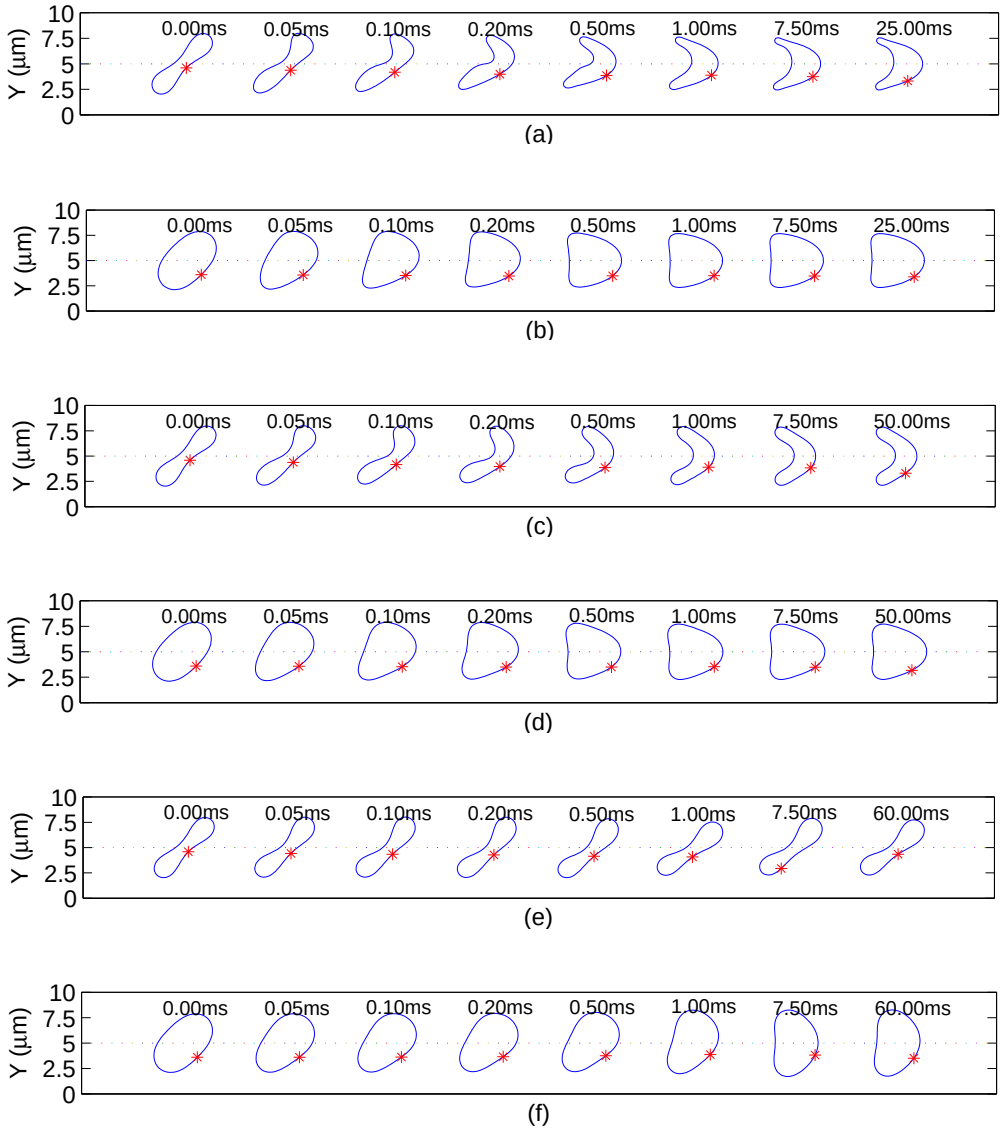

Figure 19: (Color online). The snapshots of the cell motion in Poiseuille flows for $s^* = 0.481$ and 0.9 with different bending constants: (a) $s^* = 0.481$ and $0.1k_b$, (b) $s^* = 0.9$ and $0.1k_b$, (c) $s^* = 0.481$ and $1k_b$, (d) $s^* = 0.9$ and $1k_b$, (e) $s^* = 0.481$ and $10k_b$, and (f) $s^* = 0.9$ and $10k_b$. The red asterisk denotes the same node point on the cell membrane. u_{max}=7.5 cm/s.

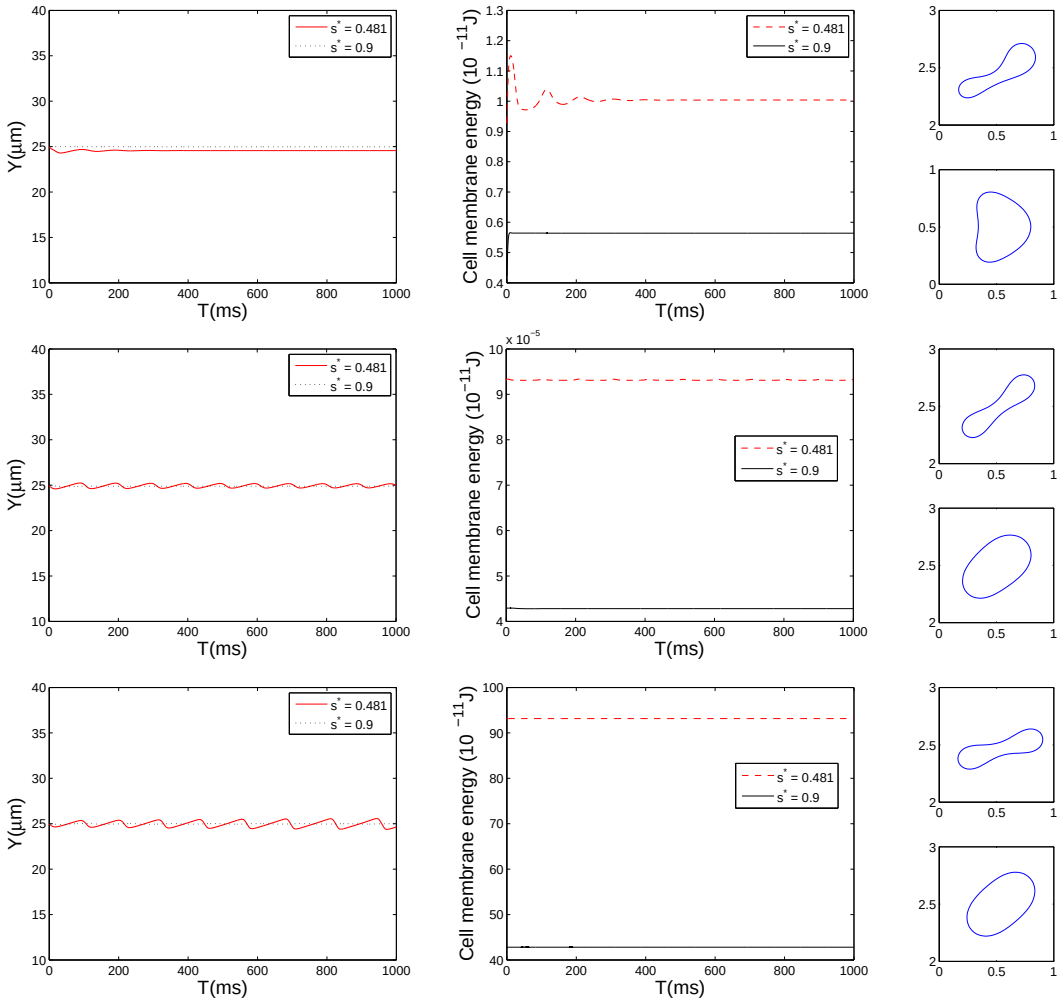

Figure 20: (Color online). The history of the position of the cell mass center (left), the energy of the cell membrane (middle) and the equilibrium shape(right) for various bending constants: 0.1 k_b (top), 1 k_b (middle), 10 k_b (bottom).

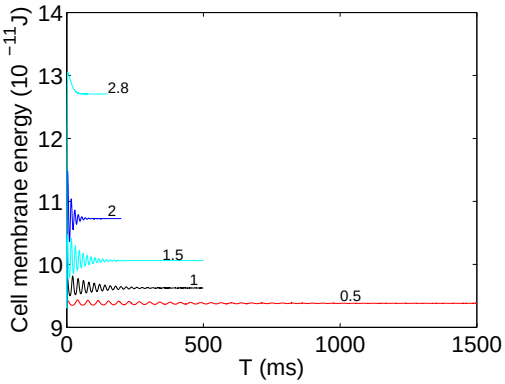

Figure 21: (Color online). The cell membrane energy for $s^* = 0.481$ with different values $u_{max} = 0.5$, 1.0, 1.5, 2.0, 2.8 cm/s.

shape and bulletlike shape, depending on the angle φ, coexist for the elliptic shape cell with lower u_{max} in a narrower channel.

Our simulation method has been also applied to the cases of multi-cells [32, 33]. Studying the deformation and other dynamics of RBCs with the viscosity of the cytoplasm bigger than that of the blood plasma in flow is an interesting and challenging problem and will be done in near future.

Acknowledgments

This work is supported by an NSF grant DMS-0914788. We acknowledge the helpful comments of James Feng, Ming-Chih Lai and Sheldon X. Wang.

References

[1] T. M. Fischer, *Biophys. J.*, **86**, 3304 (2004).

[2] P. B. Canham, and A. C. Burton, *Cir.Res.*, **22**, 405 (1968).

[3] C. H. Wang, and A. S. Popel, *Math. Biosci.*, **116**, 89 (1993).

[4] A. M. Dondorp, B. J. Angus, K. Chotivanich, K. Silamut, R. Ruangveerayuth, M. R. Hardeman, P. A. Kager, J. Vreeken, and N. J. White, *American Journal of Tropical Medicine and Hygiene*, **60-5**, 733 (1999).

[5] N. Mohandas, W. M. Phillips, and M. Bessis, *Semin. Hematol.*, **16**, 95 (1979).

[6] T. M. Fischer, M. Stöhr-Liesen, and H. Schmid-Schönbein, *Science*, **202**, 894 (1978).

[7] S. R. Keller, and R. Skalak, *J. Fluid Mech.*, **120**, 27 (1982).

[8] H. B. Li, H. H. Yi, X. M. Shan, and H. P. Fang, *Europhysics Letters*, **81**, 54002 (2008).

[9] K. H. Haas, C. Blom, D. Ende, M. H. G. Duits, and J. Mellema, *Phys. Rev. E*, **56**, 7132 (1997).

[10] R. Bruinsma, *Phys. A.*, **234**, 249 (1996).

[11] S. Huang, T. W. Pan, C. C. Chu, and C. C. Chang, *in preparation.*

[12] B. Kaoui, J. Harting, and C. Misbah, *Phys. Rev. E*, **83**, 066319 (2011).

[13] C. Misbah, *Phys. Rev. Lett.*, **96**, 028104 (2006).

[14] H. Noguchi, and G. Gompper, *Phys. Rev. Lett.*, **98**, 128103 (2007).

[15] T. W. Pan, and T. Wang, *International Journal of Numerical Analysis and Modeling*, **6**, 455 (2009).

[16] C. Eggleton, and A. Popel, *Phys. Fluids*, **10**, 1834 (1998).

[17] V. Kantsler, and V. Steinberg, *Phys. Rev. Lett.*, **96**, 036001 (2006).

[18] G. Coupier, B. Kaoui, T. Podgorski, and C. Misbah, *Physics of Fluids*, **20**, 111702 (2008).

[19] G. Danker, P. M. Vlahovska, and C. Misbah, *Phys. Rev. Lett.*, **102**, 148102 (2009).

[20] C. Pozrikidis, *Ann. Biomed. Eng.*, **33**, 165 (2005).

[21] B. Kaoui, G. Biros, and C. Misbah, *Phys. Rev. Lett.*, **103**, 188101 (2009).

[22] J. S. Park, S. H. Song, and H. Jung, *The Royal Society of Chemistry*, **9**, 939 (2009).

[23] S. Mortazavi, and G. Tryggvason, *J.Fluid. Mech.*, **411**, 325 (2000).

[24] S. J. Shin, and H. J. Sung, *Phys. Rev. E*, **83**, 046321 (2011).

[25] H. Noguchi, and G. Gompper, *PNAS.*, **no.40**, 14159 (2005).

[26] K. Tsubota, S. Wada, and T. Yamaguchi, *J. Biomech. Sci. Eng.*, **1**, 159 (2006).

[27] E. J. Dean, and R. Glowinski, *C.R. Acad. Sc. Paris, Série 1*, **325**, 783 (1997).

[28] E. J. Dean, R. Glowinski, and T. W. Pan, *Mathematical and Numerical Aspects of Wave Propagation*, De Santo JA (Ed.), SIAM: Philadelphia, 65 (1998).

[29] R. Glowinski, *Handbook of Numerical Analysis*, Vol. IX, Ciarlet PG and Lions JL (Eds.), North-Holland: Amsterdam, 7 (2003).

[30] R. Glowinski, T. W. Pan, T. Hesla, D. D. Joseph, and J. Periaux, *J. Comput. Phys.*, **169**, 363 (2001).

[31] T. W. Pan, and R. Glowinski, *Computational Fluid Dynamics Journal*, **9**, 28 (2000).

[32] T. W. Pan, L. Shi, and R. Glowinski, *Chinese Annals of Mathematics, Series B*, **31**, 975 (2010).

[33] L. Shi, T. W. Pan, and R. Glowinski, *International Journal for Numerical Methods in Fluids*, (available online) (2010).

[34] J. Adams, P. Swarztrauber, and R. Sweet, FISHPAK: A package of Fortran subprograms for the solution of separable elliptic partial differential equations, The National Center for Atmospheric Research, Boulder, CO, 1980.

[35] C. S. Peskin, *J. Comput. Phys.*, **25**, 220 (1977).

[36] C. S. Peskin, and D. M. McQueen, *J. Comput. Phys.*, **37**, 11332 (1980).

[37] C. S. Peskin, The immersed boundary method, *Acta Numer.*, **11**, 479 (2002).

[38] E. J. Ding, and C. K. Aidun, *J. Fluid Mech.*, **423**, 317 (2000).

[39] C. M. Zettner, and M. Yoda, *J.Fluid Mech.*, **442**, 241 (2001).

[40] J. Beaucourt, F. Rioual, T. Séon, T. Biben, and C. Misbah, *Phys. Rev. E*, **9**, 011906 (2004).

[41] C. Pozrikidis *Phys. Fluids*, **17**, 031503 (2005).

[42] T. W. Secomb, and R. Skalak, *Microvasc. Res.*, **24**, 194 (1982).

[43] R. Skalak and P. I. Branemark, *Science*, **164**, 717 (1969).

[44] B. Kaoui, N. Tahiri, T. Biben, H.Ez-Zahraouy, A. Benyoussef, G. Biros, and C. Misbah, *Phys. Re. E*, **84**, 041906 (2011).